

Transient dynamics of associative memory models

David G. Clark*

Zuckerman Institute, Columbia University, New York, NY 10027, USA and
Kavli Institute for Brain Science, Columbia University, New York, NY 10027, USA

(Dated: June 10, 2025)

Associative memory models such as the Hopfield network and its dense generalizations with higher-order interactions exhibit a “blackout catastrophe”—a discontinuous transition where stable memory states abruptly vanish when the number of stored patterns exceeds a critical capacity. This transition is often interpreted as rendering networks unusable beyond capacity limits. We argue that this interpretation is largely an artifact of the equilibrium perspective. We derive dynamical mean-field equations using a bipartite cavity approach for graded-activity dense associative memory models, with the Hopfield model as a special case, and solve them using a numerical scheme. We show that patterns can be transiently retrieved with high accuracy above capacity despite the absence of stable attractors. This occurs because slow regions persist in the above-capacity energy landscape as shallow, unstable remnants of below-capacity stable basins. The same transient-retrieval effect occurs in below-capacity networks initialized outside basins of attraction. “Transient-recovery curves” provide a concise visual summary of these effects, revealing graceful, non-catastrophic changes in retrieval behavior above capacity and allowing us to compare the behavior across interaction orders. This dynamical perspective reveals rich energy landscape structure obscured by equilibrium analysis and suggests biological neural circuits may exploit transient dynamics for memory retrieval. Furthermore, our approach suggests ways of understanding computational properties of neural circuits without reference to fixed points, advances the technical repertoire of numerical mean-field solution methods for recurrent neural networks, and yields new theoretical results on generalizations of the Hopfield model.

I. INTRODUCTION

The Hopfield model is a recurrent neural network with weights constructed through a Hebbian learning rule that can store and retrieve patterns, therefore functioning as a memory device [1, 2]. Its dynamics are governed by an energy function, enabling its analysis within equilibrium statistical mechanics, in particular, using methods for disordered systems such as the replica method [3, 4].

A key result from this line of work is that the standard Hopfield model can successfully store and retrieve $P = \mathcal{O}(N)$ random patterns as stable fixed points, where N is the number of neurons. Beyond this capacity, interference among patterns encoded in the connectivity destroys these stable states [3, 4], a phenomenon known as “blackout catastrophe” [5, 6]. This represents a discontinuous, first-order phase transition: the overlap between network activity and a target pattern remains high, corresponding to memory retrieval, until a critical capacity of $P \approx 0.14N$ for binary-spin models. Beyond this capacity, the high-overlap solution vanishes and only the zero-overlap solution remains.

The limited capacity of the Hopfield model has motivated various generalizations. The dense associative memory model, recently revived by Krotov and Hopfield [7, 8] but introduced and studied decades earlier [9–12], achieves capacity $P = \mathcal{O}(N^n)$ using $(n+1)$ -way neuronal interactions. This represents a qualitative improvement over the Hopfield model’s $P = \mathcal{O}(N)$ capacity

for $n > 1$, with the Hopfield model corresponding to the special case $n = 1$ with pairwise interactions. These generalized models thus liberate storage capacity from pattern dimensionality, which are constrained to be proportional in the Hopfield case. A caveat to this line of work is that while the model achieves $P = \mathcal{O}(N^n)$ capacity, it can equivalently be formulated as a bipartite system with $P + N$ units using pairwise interactions, thus recovering linear scaling in the total number of units. Rather than appealing to this bipartite formulation, biological implementations of effectively higher-order neuronal interactions have been proposed, but remain speculative [13]. Regardless of how significant one finds the increased capacity, what remains interesting and nontrivial are the *pattern retrieval dynamics*, the focus of this work, that allow these models to recall stored patterns from partial or corrupted inputs within densely packed feature spaces.

Like the Hopfield model, these generalized models possess energy functions governing their dynamics and exhibit discontinuous vanishing of stable retrieval states when capacity is exceeded [9], though this is less limiting in practice given their increased capacity for $n > 1$.

The capacity constraints that seemingly render associative memory models unusable beyond their capacity limits are derived from equilibrium analyses that probe stable memory states, i.e., energy landscape local minima, but provide limited insight into the system’s behavior during transient evolution. We therefore adopt a dynamical rather than equilibrium perspective on associative memory models. We study the out-of-equilibrium, transient dynamics of these systems and demonstrate that the blackout catastrophe is not catastrophic when viewed dynamically. In particular, even when stable fixed

* dgc2138@cumc.columbia.edu

points no longer exist beyond the critical capacity, memories can still be transiently recalled, often with high accuracy, during evolution from initial conditions. Analysis of the energy function reveals that this transient retrieval reflects the presence of slow regions in the energy landscape—remnants of below-capacity fixed points that persist in the above-capacity regime and allow temporary recall before the system is eventually driven away.

Neural circuit dynamics are frequently characterized through fixed points and stability analysis. Constructing a “dynamical skeleton” based on fixed points and transitions between them has been among the most successful approaches for understanding recurrent neural networks [14] and biological neural circuits [15]. However, transient dynamics outside of fixed points are likely crucial for neural computation and require new analytical methods [16]. For memory networks, we propose “transient-recovery curves,” which characterize memory retrieval performance without requiring stable attractor states. These curves reveal a graceful degradation of retrieval performance as capacity is exceeded, rather than abrupt failure. By varying the number of stored patterns, these curves sweep out a family that can be compared across different interaction orders n , providing insight into how higher-order interactions shape retrieval dynamics.

To study these transient dynamics in the $N \rightarrow \infty$ limit, we develop a dynamical mean-field theory for graded-activity dense associative memory models storing an appropriately scaled infinite number of patterns [17]. We solve the resulting self-consistent equations using iterative numerical methods similar to those described by Roy *et al.* [18] for ecological systems. The equilibrium statistical mechanics of graded-activity Hopfield networks (the $n = 1$ case) was analyzed by Kühn *et al.* [19]. While several works from the 1980s and 1990s derived dynamical

mean-field equations for Hopfield networks, they typically studied binary spins rather than continuous variables and, more importantly, could not numerically solve the full self-consistent equations. We review this historical context in detail in the Discussion. The iterative scheme we use here is made feasible by modern computational resources, particularly GPU acceleration. Our approach enables us to capture the full temporal evolution of these systems, reveals rich transient dynamics that were previously inaccessible to theoretical analysis, and extends all of these analyses to higher-order generalizations of the Hopfield model.

II. HOPFIELD AND DENSE ASSOCIATIVE MEMORY MODELS

We now define the class of models considered in this paper: the dense associative memory model for arbitrary interaction order n , with the Hopfield model corresponding to $n = 1$. We then specify a generative process for the stored patterns and initial conditions to enable a large- N analysis. Finally, we distinguish between condensed and uncondensed patterns and show through a signal-to-noise argument that the capacity scales as $P = \mathcal{O}(N^n)$.

A. Neuronal formulation

The dense associative memory model generalizes the Hopfield model by introducing higher-order interactions between neurons (Fig. 1a). Consider N neurons with preactivations $x_i(t)$ and nonlinearly transformed activations $\phi_i(t) = \phi(x_i(t))$, where $i \in \{1, 2, \dots, N\}$ indexes neurons and $\phi(x)$ is a bounded and monotonic neuronal nonlinearity. The neuronal dynamics are governed by

$$x_i(t) = (1 - \Delta t)x_i(t - 1) + \Delta t \left[\frac{g}{\sqrt{\alpha}} \sum_{j_1, j_2, \dots, j_n} T_{i j_1 j_2 \dots j_n} \phi_{j_1}(t - 1) \phi_{j_2}(t - 1) \dots \phi_{j_n}(t - 1) + I_i(t - 1) \right], \quad (1)$$

where $t \in \{1, 2, \dots, T\}$ indexes discrete time steps, Δt is the time step size, and $I_i(t)$ are external inputs that serve as source terms in the mean-field analysis (they can be set to zero when not needed for this purpose). The interaction tensor is constructed from P stored patterns ξ_i^μ , where $\mu \in \{1, 2, \dots, P\}$ indexes patterns, via

$$T_{i j_1 j_2 \dots j_n} = \frac{1}{N^n} \sum_{\mu} \xi_i^\mu \xi_{j_1}^\mu \xi_{j_2}^\mu \dots \xi_{j_n}^\mu. \quad (2)$$

The memory load parameter, which appears in the dynamics (Eq. 1), is defined as

$$\alpha = \frac{P}{N^n}. \quad (3)$$

This formulation involves $(n + 1)$ -way interactions among neurons. For $n = 1$, we recover the Hopfield model with pairwise interactions through the matrix

$$T_{ij} = \frac{1}{N} \sum_{\mu} \xi_i^\mu \xi_j^\mu, \quad (4)$$

which can be formed via Hebbian learning with ξ_j^μ and ξ_i^μ pre- and postsynaptic activity, respectively.

As $\Delta t \rightarrow 0$ while holding the total time $T\Delta t$ fixed, we

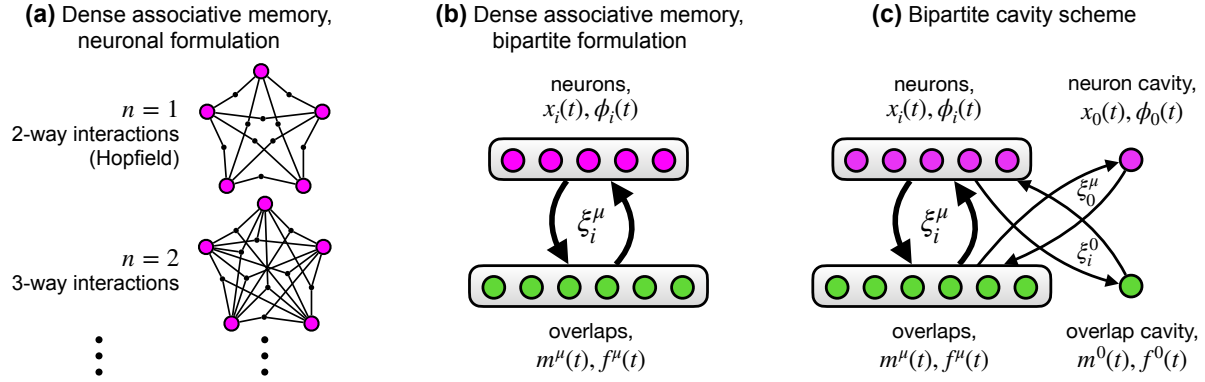


FIG. 1. Schematics of the dense associative memory model. (a) Neuronal formulation with higher-order interactions. Nodes represent neurons and black dots indicate connections (i.e., tensor elements $T_{ij_1 \dots j_n}$) (b) Equivalent formulation as a bipartite network with neurons $x_i(t)$ and overlaps $m^\mu(t)$ connected in a bipartite manner through stored patterns ξ_i^μ . (c) Schematic of bipartite cavity scheme used to derive the DMFT.

obtain the continuous-time limit of the dynamics,

$$(1 + \partial_t)x_i(t) = \frac{g}{\sqrt{\alpha}} \sum_{j_1, j_2, \dots, j_n} T_{ij_1 j_2 \dots j_n} \times \phi_{j_1}(t)\phi_{j_2}(t) \dots \phi_{j_n}(t) + I_i(t), \quad (5)$$

for which an energy can be defined (Sec. III D) [7, 8].

B. Bipartite formulation

This system with higher-order interactions among neurons can be equivalently represented as a bipartite system of neurons and overlaps (Fig. 1b). This reformulation proves advantageous for several reasons. First, it provides a pathway for implementing such models using biological neurons and synapses. Second, the bipartite structure lends itself well to the cavity method, which we use to derive the DMFT (Fig. 1c).

We introduce P overlaps $m^\mu(t)$ defined as

$$m^\mu(t) = \frac{1}{N} \sum_i \xi_i^\mu \phi_i(t) + I^\mu(t), \quad (6)$$

where $I^\mu(t)$ are external inputs to the overlaps that serve as source terms in the mean-field analysis. Like the neuronal source terms, they can be set to zero when not needed for this purpose. The overlap $m^\mu(t)$ measures the alignment between the network state at time t , $\phi_i(t)$, and the μ -th stored pattern, ξ_i^μ . In analogy with the neuronal nonlinearity, we define nonlinearly transformed overlaps as $f^\mu(t) = f(m^\mu(t))$, where $f(m)$ is a polynomial:

$$f(m) = m^n, \quad n \geq 1. \quad (7)$$

The neuronal dynamics of Eq. 1 can then be written as

$$x_i(t) = (1 - \Delta t)x_i(t - 1) + \Delta t \left[\frac{g}{\sqrt{\alpha}} \sum_\mu \xi_i^\mu f^\mu(t - 1) + I_i(t - 1) \right]. \quad (8)$$

In this bipartite representation, neurons and overlaps interact through couplings given by the stored patterns ξ_i^μ . The Hopfield model corresponds to the case where nonlinearity appears only in the neuronal variables (since, in this case, $f(m) = m$). The dense associative memory model is thus a natural generalization where a pointwise nonlinearity $f(m)$ is also applied to the overlaps.

An interesting extension of these models, that we do not pursue here, is to give the overlaps relaxational dynamics with their own timescale rather than following the instantaneous equation Eq. 6. Moreover, the overlaps can have more complex nonlinearities, including nonlinearities that couple different overlaps to each other, while preserving the existence of an energy function. This reveals connections to self-attention mechanisms [8].

C. Pattern and initial-condition statistics

To analyze the large- N limit, we specify a generative process for the patterns ξ_i^μ , which act as quenched disorder. We adopt the standard assumption of independent and identically distributed pattern components:

$$\xi_i^\mu \stackrel{\text{iid}}{\sim} P(\xi), \quad (9)$$

where $P(\xi)$ is a probability distribution with zero mean and variance σ_ξ^2 .

To study pattern retrieval, we initialize the network with significant overlap with a finite number of patterns of interest, plus random noise. Let $\mu^* \in \{1, 2, \dots, s\}$ index s patterns of interest, where s is finite and typically small (e.g., $s = 1$). Neurons are initialized as

$$x_i(1) = \sum_{\mu^*} a^{\mu^*} \xi_i^{\mu^*} + z_i, \quad (10)$$

where a^{μ^*} are coefficients determining the initial overlap with pattern μ^* , and z_i represents random noise inde-

pendent of the patterns:

$$z_i \stackrel{\text{iid}}{\sim} P(z), \quad (11)$$

with $P(z)$ having zero mean and variance σ_z^2 .

D. Capacity and condensed patterns

We now justify the capacity scaling $P = \mathcal{O}(N^n)$ through a signal-to-noise analysis. For this scaling to yield interesting dynamics (e.g., phase transitions at $\mathcal{O}(1)$ values of α), the signal from the finite number of patterns of interest and the noise from all other patterns encoded in the weights must compete on equal footing.

A key insight underlying the work of Amit, Gutfreund, and Sompolinsky [3, 4] is that pattern overlaps have two possible scalings with N , which they referred to as condensed and uncondensed patterns. These correspond to signal and noise, respectively:

$$m^\mu(t) = \begin{cases} \mathcal{O}(1) & \text{condensed patterns,} \\ \mathcal{O}(1/\sqrt{N}) & \text{uncondensed patterns.} \end{cases} \quad (12)$$

The $\mathcal{O}(1)$ overlap signifies that the neuronal state is non-trivially aligned with the corresponding condensed pattern. By contrast, the $\mathcal{O}(1/\sqrt{N})$ overlap for an uncondensed pattern corresponds to the typical inner product, divided by N , between two random, independent vectors of dimension N . While this scaling is what one obtains for independent vectors, uncondensed patterns *do* influence the neuronal state—assuming complete independence between the neuronal state and all patterns would yield incorrect mean-field equations. In modern parlance, condensed and uncondensed patterns relate to rich and lazy regimes of neural-network activity, respectively [20].

The s patterns used to initialize the network (as described in Sec. II C) become the condensed patterns, since they are initialized with $\mathcal{O}(1)$ overlap and maintain this scaling throughout the dynamics. The other $P - s$ patterns remain uncondensed, as patterns initialized with $\mathcal{O}(1/\sqrt{N})$ overlap cannot transition to condensed status on $\mathcal{O}(1)$ timescales.

The neuronal input from stored patterns is given by $\frac{g}{\sqrt{\alpha}} \sum_\mu \xi_i^\mu f^\mu(t)$ (Eq. 8). There are s condensed patterns and $P - s$ uncondensed patterns, where s is finite, $P = \alpha N^n$, and $N \rightarrow \infty$. For condensed patterns, we have $f^\mu(t) = [m^\mu(t)]^n = \mathcal{O}(1)$, giving an $\mathcal{O}(1)$ contribution to the neuronal input.

Each uncondensed pattern contributes much less individually than condensed patterns, but there are many more of them. Since $m^\mu(t) = \mathcal{O}(1/\sqrt{N})$ for uncondensed patterns, we have $f^\mu(t) = [m^\mu(t)]^n = \mathcal{O}(1/N^{n/2})$. To estimate the total contribution from uncondensed patterns, we treat the quenched disorder ξ_i^μ and dynamic variables $f^\mu(t)$ as independent. While this approximation would yield incorrect mean-field equations, as mentioned above,

it suffices for determining the correct scaling behavior. The input from uncondensed patterns has zero mean, and its magnitude scales as

$$\underbrace{\frac{g}{\sqrt{\alpha}}}_{\text{prefactor}} \times \underbrace{\sqrt{P}}_{\text{num. terms in sum}} \times \underbrace{\frac{\sigma_\xi}{N^{n/2}}}_{\text{size of each term}} = g\sigma_\xi, \quad (13)$$

where we have used $P = \alpha N^n$. This shows that the noise contribution from uncondensed patterns is also $\mathcal{O}(1)$, confirming that signal and noise compete on equal footing for the chosen scaling $P = \alpha N^n$.

III. DYNAMICAL MEAN-FIELD THEORY (DMFT)

To analyze the transient dynamics of these models in the large- N limit, we develop a DMFT. Unlike traditional equilibrium approaches that focus on fixed points and their stability, DMFT captures the full time evolution of the system, including out-of-equilibrium states where the most interesting memory retrieval properties emerge.

A. Order parameters

The DMFT involves three types of order parameters that characterize macroscopic network activity. The first is the two-time correlation function of neuronal activations,

$$C^\phi(t, t') = \frac{1}{N} \sum_i \phi_i(t) \phi_i(t'). \quad (14)$$

The second is the response function,

$$S^\phi(t, t') = \frac{1}{N} \sum_i \frac{d\phi_i(t)}{dI_i(t')}, \quad (15)$$

which measures how neuronal activations at time t respond to infinitesimal perturbations of the source term $I_i(t')$ at time t' . The third consists of the overlaps with the s condensed patterns used to initialize the dynamics,

$$m^{\mu^*}(t) = \frac{1}{N} \sum_i \xi_i^{\mu^*} \phi_i(t). \quad (16)$$

The DMFT consists of self-consistent equations that determine these order parameters in the limit $N \rightarrow \infty$. Finite-size, large- N simulations are expected to match these limiting values up to $\mathcal{O}(1/\sqrt{N})$ fluctuations.

B. Approaches

Two main approaches exist for deriving DMFT equations for disordered dynamical systems: path-integral methods and cavity methods. Both approaches address

the central challenge that quenched disorder (stored patterns) and dynamic variables (neurons and overlaps) are correlated, making naive disorder averaging incorrect (despite its sufficiency for computing scaling behavior as done above). In the Discussion, we review path integral methods in detail, as they are the basis of most prior work on the DMFT of Hopfield models.

In this paper we use the cavity method, which provides a more intuitive approach for handling correlations between quenched disorder and dynamic variables. The central idea is to remove a dynamic variable from the system (creating the titular cavity), then reintroduce it to analyze its effect on the network perturbatively. This approach is particularly well-suited for bipartite systems [21, 22] like our neuron-overlap formulation.

The cavity procedure consists of four steps (Fig. 1c):

1. Begin with an unperturbed system of dynamic variables for a given realization of quenched disorder.
2. Couple a new “cavity” variable to the existing variables via new random couplings. The cavity variable’s introduction perturbs the existing variables.
3. Write the dynamic equation for the cavity variable, where the input it receives from other variables accounts for how those variables are perturbed in response to the cavity variable’s introduction. This perturbation generates a self-coupling term in the resulting single-site dynamics.
4. Average over the quenched disorder to obtain statistics of the quantities appearing in this single-site picture. The cavity construction allows these averages to be computed because, in the expressions of interest, the quenched disorder is independent of the dynamic variables—the dynamic variables were already defined for the original system

before the new random couplings to the cavity variable were introduced.

The bipartite structure of the system further simplifies this analysis. When introducing a cavity variable (either a neuron or an overlap), we only need to compute its effect on the opposite type of variables (overlaps or neurons, respectively), since only the opposite type provides direct input to the cavity variable. We perform the cavity analysis twice—once with a neuron cavity and once with an overlap cavity—producing two complementary pictures. The self-consistent equations in each picture depend on statistical averages from the other, creating a closed, mutually referential system that determines the order parameters.

The calculation used here is “zero temperature” in the sense that they dynamic variables follow deterministic evolution given the quenched disorder. Such zero-temperature cavity methods [23] have been applied to static problems, including problems with a bipartite structure [24, 25]. For a cavity calculation of the Hopfield equilibrium properties at finite temperature, see [26].

C. Derivation using the cavity method

1. Neuron cavity

We now derive the DMFT using the bipartite cavity method. We first add a “cavity neuron” $x_0(t)$ with activation $\phi_0(t)$ to the system. This neuron connects to all existing overlaps through new random couplings ξ_0^μ . The addition of this neuron perturbs the overlaps of uncondensed patterns by

$$\delta f^\mu(t) = \sum_{t'} \sum_\nu \frac{df^\mu(t)}{dI^\nu(t')} \frac{1}{N} \xi_0^\nu \phi_0(t'). \quad (17)$$

The dynamic equation for the cavity neuron, including feedback in response to its own presence, is

$$x_0(t) = (1 - \Delta t)x_0(t-1) + \Delta t \left[\underbrace{\frac{g}{\sqrt{\alpha}} \sum_{\mu^*} \xi_0^{\mu^*} f^{\mu^*}(t-1)}_{\text{from condensed patterns}} + \underbrace{\frac{g}{\sqrt{\alpha}} \sum_\mu \xi_0^\mu f^\mu(t-1)}_{= \eta_0(t-1), \text{ neuronal cavity field}} + \sum_{t'} \underbrace{\left[\frac{g}{\sqrt{\alpha}N} \sum_{\mu, \nu} \xi_0^\mu \xi_0^\nu \frac{df^\mu(t-1)}{dI^\nu(t')} \right]}_{= F_{00}(t-1, t'), \text{ neuronal self-coupling kernel}} \phi_0(t') + I_0(t-1) \right], \quad (18)$$

where we have separated the contributions from condensed patterns μ^* and defined the neuronal cavity field and self-coupling kernel. If we know the disorder-averaged moments of these quantities, we can proceed with the analysis.

The central advantage of the cavity construction is that, as described in step 4 above, it decouples the

quenched disorder ξ_0^μ from the dynamic variables $f^\mu(t)$ and $df^\mu(t)/dI^\nu(t')$, enabling us to evaluate disorder-averaged moments of the cavity field and self-coupling kernel. By the central limit theorem, the neuronal cavity

field $\eta_0(t)$ is Gaussian with statistics

$$\langle \eta_0(t) \rangle = \frac{g}{\sqrt{\alpha}} \sum_{\mu} \underbrace{\langle \xi_0^\mu \rangle}_{=0} \langle f^\mu(t) \rangle = 0, \quad (19)$$

$$\begin{aligned} \langle \eta_0(t) \eta_0(t') \rangle &= \frac{g^2}{\alpha} \sum_{\mu, \nu} \underbrace{\langle \xi_0^\mu \xi_0^\nu \rangle}_{=\delta^{\mu\nu} \sigma_\xi^2} \langle f^\mu(t) f^\nu(t') \rangle \\ &= g^2 \sigma_\xi^2 N^n \langle f^\mu(t) f^\mu(t') \rangle. \end{aligned} \quad (20)$$

Noting that $f^\mu(t) = \mathcal{O}(1/N^{n/2})$, the correlation function $\langle \eta_0(t) \eta_0(t') \rangle$ is $\mathcal{O}(1)$, i.e., $\eta_0(t)$ itself is $\mathcal{O}(1)$ as expected from the scaling arguments in Sec. II D in which the decoupling achieved here using the cavity construction was instead assumed in an unjustified manner. Meanwhile, the self-coupling kernel $F_{00}(t, t')$ is $\mathcal{O}(1)$ and self-averaging with mean

$$\begin{aligned} F_{00}(t, t') &= \frac{g}{\sqrt{\alpha} N} \sum_{\mu, \nu} \underbrace{\langle \xi_0^\mu \xi_0^\nu \rangle}_{=\delta^{\mu\nu} \sigma_\xi^2} \left\langle \frac{df^\mu(t)}{dI^\nu(t')} \right\rangle \\ &= g \sigma_\xi^2 \sqrt{\alpha} N^{n-1} \left\langle \frac{df^\mu(t)}{dI^\mu(t')} \right\rangle. \end{aligned} \quad (21)$$

These averages depend on pattern statistics, which we determine through the complementary overlap-cavity analysis, i.e.,

$$\langle \eta_0(t) \eta_0(t') \rangle = g^2 \sigma_\xi^2 N^n \langle f^0(t) f^0(t') \rangle, \quad (22)$$

$$F_{00}(t, t') = g \sigma_\xi^2 \sqrt{\alpha} N^{n-1} \left\langle \frac{df^0(t)}{dI^0(t')} \right\rangle. \quad (23)$$

To complete the analysis, we now derive the pattern overlap-cavity equations that will allow us to compute these averages.

2. Overlap cavity

We add an overlap $m^0(t)$, for an uncondensed pattern, connected to all neurons through new random couplings ξ_i^0 . The perturbation to neurons due to this cavity overlap is

$$\delta\phi_i(t) = \sum_{t'} \sum_j \frac{d\phi_i(t)}{dI_j(t')} \frac{g}{\sqrt{\alpha}} \xi_j^0 f^0(t'). \quad (24)$$

The dynamic equation for the cavity overlap is then

$$\begin{aligned} m^0(t) &= \underbrace{\frac{1}{N} \sum_i \xi_i^0 \phi_i(t)}_{=\eta^0(t), \text{ overlap cavity field}} + \sum_{t'} \underbrace{\left[\frac{g}{\sqrt{\alpha} N} \sum_{i,j} \xi_i^0 \xi_j^0 \frac{d\phi_i(t)}{dI_j(t')} \right]}_{=F^{00}(t, t'), \text{ overlap self-coupling kernel}} f^0(t') + I^0(t), \end{aligned} \quad (25)$$

where we have defined the overlap cavity field and self-coupling kernel. As with the neuronal cavity, we use the independence of quenched disorder and dynamic variables to evaluate disorder averages. The cavity field $\eta^0(t)$ is Gaussian with statistics

$$\langle \eta^0(t) \rangle = \frac{1}{N} \sum_i \underbrace{\langle \xi_i^0 \rangle}_{=0} \langle \phi_i(t) \rangle = 0, \quad (26)$$

$$\begin{aligned} \langle \eta^0(t) \eta^0(t') \rangle &= \frac{1}{N^2} \sum_{i,j} \underbrace{\langle \xi_i^0 \xi_j^0 \rangle}_{=\delta_{ij} \sigma_\xi^2} \langle \phi_i(t) \phi_j(t') \rangle \\ &= \frac{\sigma_\xi^2}{N} C^\phi(t, t'). \end{aligned} \quad (27)$$

The correlation function $\langle \eta^0(t) \eta^0(t') \rangle$ is $\mathcal{O}(1/N)$, implying that $\eta^0(t) = \mathcal{O}(1/\sqrt{N})$, consistent with the overlap itself being $\mathcal{O}(1/\sqrt{N})$ as expected for an uncondensed pattern. Meanwhile, the self-coupling kernel is $\mathcal{O}(1)$ and

self-averaging with mean

$$\begin{aligned} F^{00}(t, t') &= \frac{g}{\sqrt{\alpha} N} \sum_{i,j} \underbrace{\langle \xi_i^0 \xi_j^0 \rangle}_{=\delta_{ij} \sigma_\xi^2} \left\langle \frac{d\phi_i(t)}{dI_j(t')} \right\rangle \\ &= \frac{g \sigma_\xi^2}{\sqrt{\alpha}} S^\phi(t, t'). \end{aligned} \quad (28)$$

Thus the overlap cavity picture's cavity field and self-coupling kernel depend on the neuronal order parameters $C^\phi(t, t')$ and $S^\phi(t, t')$, which can be determined within the neuronal cavity picture. This creates mutually referential cavity pictures that together determine the order parameters.

3. Evaluating correlation and response functions

Since we aim to determine neuronal order parameters $C^\phi(t, t')$, $S^\phi(t, t')$, and $m^{\mu^*}(t)$, it is useful to close the mean-field equations in neuronal quantities. To do this, we must evaluate the neuronal cavity-field correlation (Eq. 22) and self-coupling kernel (Eq. 23). To deal with

temporal indices, it is helpful to use the following vector and matrix notation:

- For a time-dependent scalar quantity $q(t)$ with $t \in \{1, 2, \dots, T\}$, we define the corresponding T -dimensional vector \mathbf{q} with components $[\mathbf{q}]_t = q(t)$.
- For a two-time function $M(t, t')$ with $t, t' \in \{1, 2, \dots, T\}$, we define the corresponding $T \times T$ matrix \mathbf{M} with elements $[\mathbf{M}]_{t,t'} = M(t, t')$.
- For a two-time derivative $d\psi(t)/dI(t')$, we define the corresponding $T \times T$ matrix $d\psi/d\mathbf{I}^T$ with elements $[d\psi/d\mathbf{I}^T]_{t,t'} = d\psi(t)/dI(t')$.

In this notation, [Eq. 22](#) and [Eq. 23](#) for the neuronal cavity-field correlation and self-coupling kernel, respectively, are

$$\langle \boldsymbol{\eta}_0 \boldsymbol{\eta}_0^T \rangle = g^2 \sigma_\xi^2 N^n \langle f(\mathbf{m}^0) f(\mathbf{m}^0)^T \rangle, \quad (29)$$

$$\mathbf{F}_{00} = g\sigma_\xi^2 \sqrt{\alpha} N^{n-1} \left\langle \frac{df(\mathbf{m}^0)}{d(\mathbf{I}^0)^T} \right\rangle, \quad (30)$$

where $f(\mathbf{m}^0)$ applies the nonlinearity elementwise to the vector \mathbf{m}^0 . We need to evaluate these expressions to leading order, namely $\mathcal{O}(1)$. From the overlap cavity picture, \mathbf{m}^0 obeys, in matrix notation,

$$\mathbf{m}^0 = \boldsymbol{\eta}^0 + \frac{g\sigma_\xi^2}{\sqrt{\alpha}} \mathbf{S}^\phi f(\mathbf{m}^0) + \mathbf{I}^0 \quad (31)$$

$$\text{where } \langle \boldsymbol{\eta}^0 \rangle = 0, \quad \langle \boldsymbol{\eta}^0 (\boldsymbol{\eta}^0)^T \rangle = \frac{\sigma_\xi^2}{N} \mathbf{C}^\phi. \quad (32)$$

Here, $\boldsymbol{\eta}^0$ is Gaussian and \mathbf{m}^0 is determined by solving the nonlinear equation [Eq. 31](#).

At this point, the analysis diverges between the Hopfield ($n = 1$) and higher-order models ($n > 1$). In the $n = 1$ case, the overlap equation [Eq. 31](#) is linear, which simplifies the calculations. For $n > 1$, [Eq. 31](#) is nonlinear, but the nonlinear self-interaction is smaller than $\boldsymbol{\eta}^0$ by a factor of $1/N^{(n-1)/2}$, allowing for a perturbative treatment.

Before handling each case, we derive a general expression for the response-function term $\langle d\mathbf{m}^0/d(\mathbf{I}^0)^T \rangle$ that applies to both cases. Differentiating both sides of [Eq. 31](#) with respect to \mathbf{I}^0 and solving for $d\mathbf{m}^0/d(\mathbf{I}^0)^T$ gives

$$\frac{d\mathbf{m}^0}{d(\mathbf{I}^0)^T} = \left(\mathbf{I} - \frac{g\sigma_\xi^2}{\sqrt{\alpha}} \mathbf{S}^\phi \mathcal{D}[f'(\mathbf{m}^0)] \right)^{-1}, \quad (33)$$

where $\mathcal{D}[\cdot]$ denotes a diagonal matrix with the argument vector on the diagonal when applied to a vector, or zeros

out the off-diagonal elements when applied to a matrix; \mathbf{I} is the identity matrix; and we set $\mathbf{I}^0 = \mathbf{0}$. This allows us to express [Eq. 30](#) as

$$\mathbf{F}_{00} = g\sigma_\xi^2 \sqrt{\alpha} N^{n-1} \times \left\langle \mathcal{D}[f'(\mathbf{m}^0)] \left(\mathbf{I} - \frac{g\sigma_\xi^2}{\sqrt{\alpha}} \mathbf{S}^\phi \mathcal{D}[f'(\mathbf{m}^0)] \right)^{-1} \right\rangle. \quad (34)$$

Hopfield model ($n = 1$). For the Hopfield model, due to the linearity of the overlap dynamics, we have

$$\mathbf{m}^0 = \frac{d\mathbf{m}^0}{d(\mathbf{I}^0)^T} \boldsymbol{\eta}^0, \quad (35)$$

$$\text{where } \frac{d\mathbf{m}^0}{d(\mathbf{I}^0)^T} = \left(\mathbf{I} - \frac{g\sigma_\xi^2}{\sqrt{\alpha}} \mathbf{S}^\phi \right)^{-1}. \quad (36)$$

Thus, [Eq. 29](#) becomes

$$\begin{aligned} \langle \boldsymbol{\eta}_0 \boldsymbol{\eta}_0^T \rangle &= g^2 \sigma_\xi^2 N \langle \mathbf{m}^0 (\mathbf{m}^0)^T \rangle \\ &= g^2 \sigma_\xi^2 N \left\langle \frac{d\mathbf{m}^0}{d(\mathbf{I}^0)^T} \boldsymbol{\eta}^0 (\boldsymbol{\eta}^0)^T \left(\frac{d\mathbf{m}^0}{d(\mathbf{I}^0)^T} \right)^T \right\rangle \\ &= g^2 \sigma_\xi^4 \left(\mathbf{I} - \frac{g\sigma_\xi^2}{\sqrt{\alpha}} \mathbf{S}^\phi \right)^{-1} \mathbf{C}^\phi \left(\mathbf{I} - \frac{g\sigma_\xi^2}{\sqrt{\alpha}} \mathbf{S}^\phi \right)^{-T}. \end{aligned} \quad (37)$$

Meanwhile, since $f(m) = m$, [Eq. 34](#) simplifies to

$$\mathbf{F}_{00} = g\sigma_\xi^2 \sqrt{\alpha} \left(\mathbf{I} - \frac{g\sigma_\xi^2}{\sqrt{\alpha}} \mathbf{S}^\phi \right)^{-1}. \quad (38)$$

Higher-order models ($n > 1$). For $n > 1$, the pattern equation [Eq. 31](#) is nonlinear, but, as mentioned above, the nonlinear self-coupling term $f(\mathbf{m}^0)$ is smaller than the Gaussian input $\boldsymbol{\eta}^0$ by a factor of $1/N^{(n-1)/2}$, permitting a perturbative treatment. For [Eq. 29](#), to leading order, we can replace \mathbf{m}^0 with $\boldsymbol{\eta}^0$:

$$\begin{aligned} \langle \boldsymbol{\eta}_0 \boldsymbol{\eta}_0^T \rangle &= g^2 \sigma_\xi^2 N^n \langle f(\boldsymbol{\eta}^0) f(\boldsymbol{\eta}^0)^T \rangle \\ &= g^2 \sigma_\xi^{2(n+1)} \mathbf{P}_{n,n}, \end{aligned} \quad (39)$$

where we define the matrices

$$\mathbf{P}_{n,n'} = \left\langle \mathbf{u}^n (\mathbf{u}^{n'})^T \right\rangle_{\mathbf{u} \sim \mathcal{N}(0, \mathbf{C}^\phi)}, \quad (40)$$

with powers applied elementwise.

For the response function, noting that $f'(\mathbf{m}^0) = \mathcal{O}(1/N^{(n-1)/2})$, we expand the matrix inverse in [Eq. 34](#):

$$\begin{aligned} \mathbf{F}_{00} &= g\sigma_\xi^2\sqrt{\alpha}N^{n-1} \left\langle \mathcal{D}[f'(\mathbf{m}^0)] \left(\mathcal{I} + \frac{g\sigma_\xi^2}{\sqrt{\alpha}} \mathbf{S}^\phi \mathcal{D}[f'(\mathbf{m}^0)] + \dots \right) \right\rangle \\ &= g\sigma_\xi^2\sqrt{\alpha}N^{n-1} \langle \mathcal{D}[f'(\mathbf{m}^0)] \rangle + g^2\sigma_\xi^4 \mathbf{S}^\phi \circ \langle N^{n-1} f'(\mathbf{m}^0) f'(\mathbf{m}^0)^T \rangle + \dots \end{aligned} \quad (41)$$

where \circ denotes the Hadamard product.

For odd n , $\langle f'(\mathbf{m}^0) \rangle = \mathcal{O}(1/N^{(n-1)/2})$, implying that the first term in the expansion (Eq. 41) is $\mathcal{O}(N^{(n-1)/2})$, which diverges as $N \rightarrow \infty$. Addressing this issue properly would require a careful exclusion of self-interactions in Eq. 1. In this work, we focus on even n , for which we show that this first term is $\mathcal{O}(1)$. The different scaling behaviors of the neuronal input for even and odd n can be illustrated through a simple numerical experiment (Appendix D, Fig. 7).

For even n , we use Eq. 31 to iteratively express $f'(\mathbf{m}^0)$ in terms of $\boldsymbol{\eta}^0$:

$$f'(\mathbf{m}^0) = f'(\boldsymbol{\eta}^0) + \frac{g\sigma_\xi^2}{\sqrt{\alpha}} \mathcal{D}[f''(\boldsymbol{\eta}^0)] \mathbf{S}^\phi f(\boldsymbol{\eta}^0) + \dots, \quad (42)$$

whose k -th term is $\mathcal{O}(1/N^{k(n-1)/2})$. Substitution into the first term of the \mathbf{F}_{00} expansion Eq. 41 gives

$$\begin{aligned} g\sigma_\xi^2\sqrt{\alpha}N^{n-1} \langle \mathcal{D}[f'(\mathbf{m}^0)] \rangle &= g\sigma_\xi^2\sqrt{\alpha}N^{n-1} \langle \mathcal{D}[f'(\boldsymbol{\eta}^0)] \rangle \\ &+ g^2\sigma_\xi^4 N^{n-1} \mathcal{D}[\mathbf{S}^\phi \langle f(\boldsymbol{\eta}^0) f''(\boldsymbol{\eta}^0)^T \rangle] + \dots. \end{aligned} \quad (43)$$

Since n is even, $f'(m)$ is an odd function, so $\langle f'(\boldsymbol{\eta}^0) \rangle = 0$. For the second term in the expansion Eq. 41, we need

$\langle N^{n-1} f'(\mathbf{m}^0) f'(\mathbf{m}^0)^T \rangle$. To leading order, we can replace $f'(\mathbf{m}^0)$ with $f'(\boldsymbol{\eta}^0)$. Combining these results gives

$$\begin{aligned} \mathbf{F}_{00} &= g^2\sigma_\xi^4 \left[\mathcal{D} [\mathbf{S}^\phi \langle N^{n-1} f(\boldsymbol{\eta}^0) f''(\boldsymbol{\eta}^0)^T \rangle] \right. \\ &\quad \left. + \mathbf{S}^\phi \circ \langle N^{n-1} f'(\boldsymbol{\eta}^0) f'(\boldsymbol{\eta}^0)^T \rangle \right], \end{aligned} \quad (44)$$

where $\mathcal{D}[\cdot]$ now extracts the diagonal elements. This can be written

$$\begin{aligned} \mathbf{F}_{00} &= g^2\sigma_\xi^{2(n+1)} \left[n(n-1) \mathcal{D} [\mathbf{S}^\phi \mathbf{P}_{n,n-2}] \right. \\ &\quad \left. + n^2 \mathbf{S}^\phi \circ \mathbf{P}_{n-1,n-1} \right]. \end{aligned} \quad (45)$$

4. Final self-consistent system

In the single-site picture, $x_0(t)$ evolves from an initial condition, driven by a cavity field and self-coupling. The statistics of this single-site process determine the self-coupling kernel and cavity-field correlation function.

$$x_0(1) = \sum_{\mu^*=1} a^{\mu^*} \xi_0^{\mu^*} + z_0, \quad (46)$$

$$x_0(t) = (1 - \Delta t)x_0(t-1) + \Delta t \left[\frac{g}{\sqrt{\alpha}} \sum_{\mu^*=1} \xi_0^{\mu^*} \left(m^{\mu^*}(t-1) \right)^n + \eta_0(t-1) + \sum_{t'=1}^{t-1} F_{00}(t-1, t') \phi_0(t') \right], \quad (47)$$

$$\mathbf{C}^{\eta_0} = \begin{cases} g^2\sigma_\xi^4 \left(\mathcal{I} - \frac{g\sigma_\xi^2}{\sqrt{\alpha}} \mathbf{S}^\phi \right)^{-1} \mathbf{C}^\phi \left(\mathcal{I} - \frac{g\sigma_\xi^2}{\sqrt{\alpha}} \mathbf{S}^\phi \right)^{-T} & n = 1 \\ g^2\sigma_\xi^{2(n+1)} \mathbf{P}_{n,n} & n > 1, \text{ even} \end{cases} \quad (48)$$

$$\mathbf{F}_{00} = \begin{cases} g\sigma_\xi^2\sqrt{\alpha} \left(\mathcal{I} - \frac{g\sigma_\xi^2}{\sqrt{\alpha}} \mathbf{S}^\phi \right)^{-1} & n = 1 \\ g^2\sigma_\xi^{2(n+1)} [n(n-1) \mathcal{D} [\mathbf{S}^\phi \mathbf{P}_{n,n-2}] + n^2 \mathbf{S}^\phi \circ \mathbf{P}_{n-1,n-1}] & n > 1, \text{ even} \end{cases} \quad (49)$$

The DMFT is closed by the self-consistency conditions

$$C^\phi(t, t') = \langle \phi_0(t) \phi_0(t') \rangle_{\text{single-site}}, \quad (50)$$

$$S^\phi(t, t') = \left\langle \frac{d\phi_0(t)}{dI_0(t')} \right\rangle_{\text{single-site}}, \quad (51)$$

$$m^{\mu^*}(t) = \left\langle \xi_0^{\mu^*} \phi_0(t) \right\rangle_{\text{single-site}}, \quad (52)$$

where $\langle \cdot \rangle_{\text{single-}}_{\text{site}}$ denotes averaging over the Gaussian noise realization, condensed pattern components, and initialization noise:

$$\langle \cdots \rangle_{\text{single-}}_{\text{site}} = \langle \cdots \rangle_{\substack{\eta_0 \sim \mathcal{N}(\mathbf{0}, \mathbf{C}^{\eta_0}) \\ \xi_0^{\mu^*} \stackrel{\text{iid}}{\sim} P(\xi) \text{ for } \mu^* = 1, \dots, s \\ z_0 \sim P(z)}}. \quad (53)$$

These equations form a closed system that can be solved numerically to obtain the dynamical behavior of the model in the $N \rightarrow \infty$ limit.

D. Energy function

The models we study possess energy functions that govern their dynamics [7, 8]. For a configuration of neuronal activations $\vec{\phi} = \{\phi_i\}_{i=1}^N$, the $\mathcal{O}(1)$ energy is

$$\varepsilon[\vec{\phi}] = -\frac{g}{(n+1)\sqrt{\alpha}} \sum_{\mu} (m^{\mu})^{n+1} + \frac{1}{N} \sum_i F(\phi_i), \quad (54)$$

$$\varepsilon(t) = - \left\{ \begin{array}{ll} \frac{\sqrt{\alpha}}{2g} \langle \eta_0(t) \eta_0(t) \rangle_{\text{single-}}_{\text{site}} & n = 1 \\ \langle \eta_0(t) \phi_0(t) \rangle_{\text{single-}}_{\text{site}} & n > 1, \text{ even} \end{array} \right\} - \frac{g}{(n+1)\sqrt{\alpha}} \sum_{\mu^* = 1} (m^{\mu^*}(t))^{n+1} + \langle F(\phi_0(t)) \rangle_{\text{single-}}_{\text{site}}. \quad (57)$$

We found this expression to be the most numerically stable of several equivalent formulations.

E. Numerical solution of the DMFT

We solve the self-consistent DMFT equations using an iterative procedure that samples trajectories and updates order parameters. Such an approach for a different, ecological system is detailed in [18]. The steps are as follows.

1. Initialize order parameters \mathbf{C}^{ϕ} , \mathbf{S}^{ϕ} , and \mathbf{m}^{μ^*} for $\mu^* \in \{1, 2, \dots, s\}$.
2. Sample M noise trajectories η_m , $m \in \{1, 2, \dots, M\}$, through Cholesky decomposition of \mathbf{C}^{η_0} .
3. Sample M sets of s condensed patterns $\xi_m^{\mu^*}$.
4. Forward integrate the M trajectories using the single-site dynamics to get \mathbf{x}_m and $\phi_m = \phi(\mathbf{x}_m)$, yielding updated correlation function \mathbf{C}^{ϕ} and overlaps \mathbf{m}^{μ^*} in the straightforward way (Eq. 58 and Eq. 59 below).
5. Compute an updated response function \mathbf{S}^{ϕ} (described in Sec. III E 1 below).

where $F(\phi)$ satisfies $F'(\phi) = \phi^{-1}(\phi)$ (Appendix A). The continuous-time limit of the dynamics obeys

$$\partial_t x_i(t) = -N \partial_{\phi_i} \varepsilon[\vec{\phi}(t)]. \quad (55)$$

Note that these are not gradient dynamics because the left-hand side specifies the time derivative of x_i while the right-hand side is a gradient with respect to ϕ_i . Nevertheless, $\varepsilon[\vec{\phi}]$ acts as a Lyapunov function since the energy decreases monotonically:

$$\begin{aligned} \partial_t \varepsilon[\vec{\phi}] &= \sum_i \partial_{\phi_i} \varepsilon[\vec{\phi}] \phi'_i(t) \partial_t x_i(t) \\ &= -\frac{1}{N} \sum_i \phi'_i(t) (\partial_t x_i(t))^2 \leq 0, \end{aligned} \quad (56)$$

where the inequality follows because the nonlinearity is monotonic, $\phi'(x) > 0$. In the DMFT framework, we can express the energy in terms of order parameters as

6. Update order parameters with memory factor $\gamma \in [0, 1]$:

$$\mathbf{C}_{\text{new}}^{\phi} = (1 - \gamma) \times \mathbf{C}_{\text{old}}^{\phi} + \gamma \times \frac{1}{M} \sum_m \phi_m \phi_m^T, \quad (58)$$

$$\mathbf{m}_{\text{new}}^{\mu^*} = (1 - \gamma) \times \mathbf{m}_{\text{old}}^{\mu^*} + \gamma \times \frac{1}{M} \sum_m \xi_m^{\mu^*} \phi_m, \quad (59)$$

$$\mathbf{S}_{\text{new}}^{\phi} = (1 - \gamma) \times \mathbf{S}_{\text{old}}^{\phi} + \gamma \times \mathbf{S}_{\text{tot}}^{\phi}. \quad (60)$$

7. Repeat steps 2-6 until convergence of order parameters

1. Response function computation

For each trajectory m , the response function is computed through forward integration in t for each fixed s . The computation begins at $t = s$ and proceeds forward in time:

$$\begin{aligned} S_m^x(t, s) &= (1 - \Delta t) S_m^x(t-1, s) \\ &+ \Delta t \left[\sum_{t'=s}^{t-1} F_{00}(t-1, t') \phi'_m(t') S_m^x(t', s) + \delta_{t-1, s} \right], \end{aligned} \quad (61)$$

subject to initial conditions

$$S_m^x(s, s) = 0. \quad (62)$$

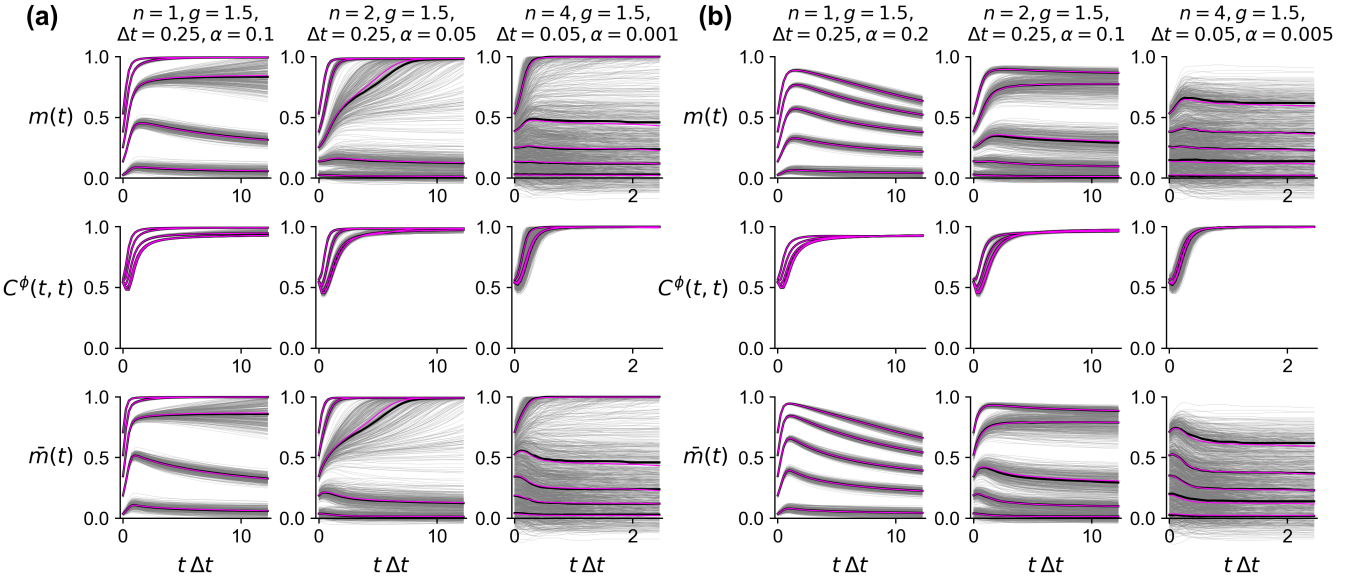


FIG. 2. Dynamical evolution of order parameters for Hopfield ($n = 1$) and dense associative memory models ($n = 2, 4$). **(a)** Below-capacity dynamics with $\alpha = 0.10, 0.05, 0.001$ for $n = 1, 2, 4$, respectively. **(b)** Above-capacity dynamics with $\alpha = 0.20, 0.10, 0.005$ for $n = 1, 2, 4$, respectively. In **(a)** and **(b)**, we show (top) raw overlap $m(t)$, (middle) equal-time correlation $C^\phi(t, t)$, and (bottom) normalized overlap $\bar{m}(t) = m(t)/(\sigma_\xi \sqrt{C^\phi(t, t)})$. Gray traces show individual finite-size simulations with $N = 20000, 2000, 200$ for $n = 1, 2, 4$, respectively; black lines show simulation medians; and magenta lines show DMFT predictions.

The equation is applied sequentially for $t = s + 1, s + 2, \dots, T$ to build up the full response function. For each trajectory, the activation response function is

$$S_m^\phi(t, s) = \phi'_m(t) S_m^x(t, s). \quad (63)$$

The final response function is obtained by averaging over all trajectories:

$$S_{\text{tot}}^\phi(t, s) = \frac{1}{M} \sum_m S_m^\phi(t, s). \quad (64)$$

We implement the numerical solution on GPU using PyTorch, enabling efficient computation with large sample sizes M . All operations are performed on GPU with the primary computational loops being the T time steps for trajectory evolution and the $T(T-1)/2$ time steps for response function integration. The $\mathcal{O}(T^2)$ response function computation dominates the runtime in practice. While the Cholesky decomposition for sampling correlated noise scales as $\mathcal{O}(T^3)$, this step negligible in comparison.

IV. RESULTS

A. Setup and equilibrium analysis

We first confirm that our model exhibits the equilibrium ‘‘blackout catastrophe’’—the discontinuous phase transition where high-overlap solutions vanish above a

critical capacity. We derive a mean-field theory for fixed-point solutions by removing the time dependencies from our DMFT equations. For the gain parameter $g = 1.5$ used throughout our analyses, we obtain critical capacities $\alpha_c \approx 0.13, 0.080$, and 0.0011 for $n = 1, 2$, and 4 , respectively. Details of this fixed-point analysis are provided in [Appendix B](#).

We restrict our analysis to interaction orders $n = 1, 2$, and 4 . Validation with finite-size simulations requires large N to reduce fluctuations that scale as $\mathcal{O}(1/\sqrt{N})$, but the scaling $P = \mathcal{O}(N^n)$ makes the number of patterns prohibitively large for $n > 4$. We exclude $n = 3$ due to the divergent behavior identified in [Sec. III](#).

All simulations and DMFT solutions focus on retrieval of a single condensed pattern, so we drop the μ^* superscript and denote the overlap as $m(t)$. We initialize the system according to [Eq. 10](#) with $a = \bar{a}g$, where $\bar{a} \in [0, 1]$ controls the initial alignment with the pattern of interest. The initialization noise level is set to $\sigma_z = \sqrt{g^2 - a^2}$ (see [Eq. 11](#)) so that the variance of the initial condition remains constant as we vary \bar{a} . By sweeping \bar{a} from 0 to 1, we explore a range of initial overlaps with the stored pattern.

For simulations, we use system sizes $N = 20000, 2000$, and 200 for $n = 1, 2$, and 4 , respectively, with time steps $\Delta t = 0.25$ for $n = 1, 2$ and $\Delta t = 0.05$ for $n = 4$ to ensure numerical stability. We examine the effects of g and Δt in the Hopfield model in [Appendix D](#).

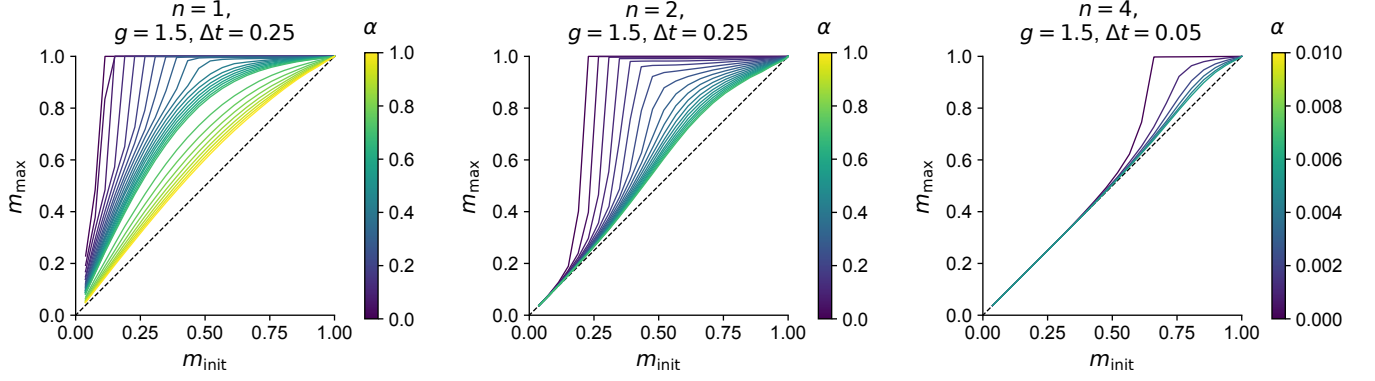


FIG. 3. Transient-recovery curves for Hopfield model ($n = 1$) and dense associative memory models ($n = 2, 4$). Each curve plots the maximum normalized overlap \bar{m}_{\max} achieved during dynamical evolution versus the initial normalized overlap \bar{m}_{init} . Different curves within each panel correspond to different memory loads $\alpha = P/N^n$. The diagonal line is the trivial lower bound where maximum overlap equals initial overlap.

B. Retrieval dynamics and key phenomena

The DMFT solutions show two types of retrieval behaviors.

Stable retrieval occurs when the overlap converges to a value independent of local variations in initial conditions. The convergence is rapid and the asymptotic overlap is close to unity, as expected from prior equilibrium analyses [3, 4, 19].

Transient retrieval occurs when the overlap initially increases during evolution but then decreases, failing to reach a stable retrieval state. This can occur either when networks exceed capacity or when they are initialized outside basins of attraction. The initial increase is fast, while the eventual decay is much slower. In cases with slow decay, the late-time overlap value appears to remain nonzero, consistent with the “remnant overlap” found in simulations of binary-neuron Hopfield models [4]. We cannot determine the exact asymptotic value of this remnant overlap because the decay is extremely slow and our numerical solver has $\mathcal{O}(T^2)$ time complexity per iteration.

Unlike networks of binary neurons, the time-dependent variance $C^\phi(t, t)$ is non-trivial, and changes in the overlap $m(t)$ reflect both changes in alignment with the pattern and changes in the variance of the neuronal state. We therefore focus on the normalized overlap,

$$\bar{m}(t) = \frac{m(t)}{\sigma_\xi \sqrt{C^\phi(t, t)}}, \quad (65)$$

which lies in $[-1, 1]$. We define $\bar{m}_{\text{init}} = \bar{m}(1)$ as the initial normalized overlap.

C. Validation and main results

We first verify that DMFT solutions match finite-size simulations. Fig. 2 demonstrates excellent agreement be-

tween theory and simulations for the overlap $m(t)$, equal-time correlation function $C^\phi(t, t)$, and normalized overlap $\bar{m}(t)$.

The normalized overlap exhibits two regimes:

Below capacity ($\alpha < \alpha_c$): When \bar{m}_{init} is sufficiently large, $\bar{m}(t)$ converges to a stable retrieval state with rapid convergence and final values close to unity. For smaller \bar{m}_{init} , $\bar{m}(t)$ transiently increases then decays slowly. Thus, even when initialized outside the basin of attraction, patterns can still be transiently recalled.

Above capacity ($\alpha > \alpha_c$): No initial overlap \bar{m}_{init} is sufficiently large to elicit stable retrieval. Instead, we observe transient retrieval for all \bar{m}_{init} . However, contrary to the equilibrium picture predicting abrupt breakdown, maximum normalized overlaps achieved can be quite high. Since the transient increase is fast and subsequent decay much slower, this behavior can resemble stable retrieval from the below-capacity regime, with the key difference being eventual slow decay rather than convergence to a stable state.

D. Transient-recovery curves

To quantify memory retrieval performance beyond stable attractors, we introduce *transient-recovery curves*. These curves characterize a network’s ability to recall stored patterns by plotting the maximum normalized overlap achieved during the entire dynamical evolution,

$$\bar{m}_{\max} = \max_t \bar{m}(t), \quad (66)$$

as a function of the initial normalized overlap \bar{m}_{init} . Each curve captures the best retrieval performance accessible through transient dynamics, regardless of whether this optimal retrieval occurs at a stable fixed point or during a transient. Fig. 3 shows these transient-recovery curves for the Hopfield model and dense associative memory models with $n = 2$ and $n = 4$, where each curve corresponds to a different memory load α .

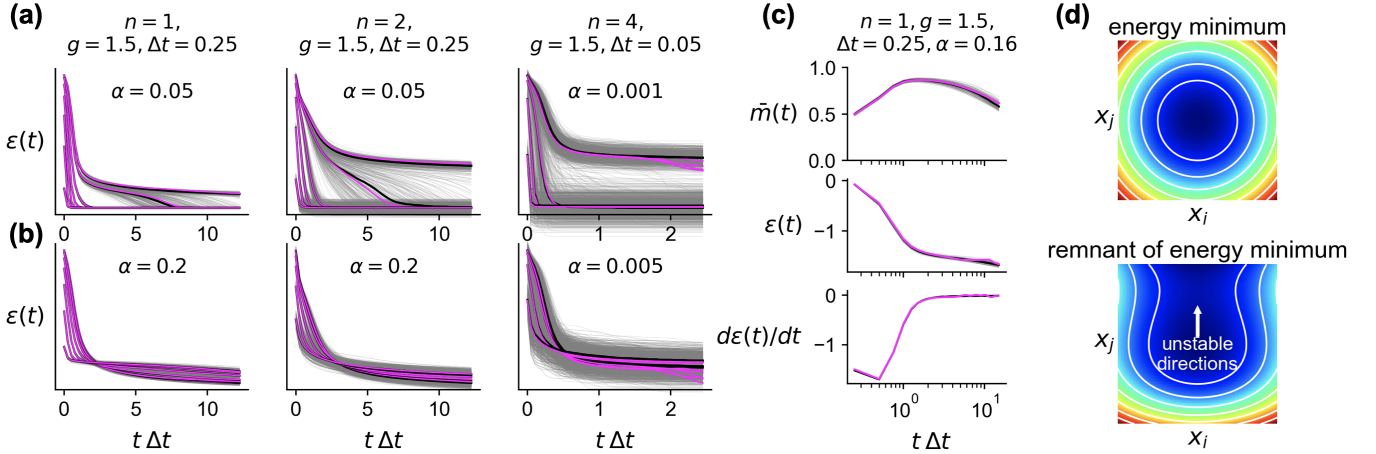


FIG. 4. Energy dynamics for different initial overlaps. (a) Below-capacity dynamics with $\alpha < \alpha_c$. (b) Above-capacity dynamics with $\alpha > \alpha_c$. In (a) and (b), columns show $n = 1, 2, 4$ from left to right. Different curves in each panel correspond to different initial normalized overlaps \bar{m}_{init} . Gray traces show individual finite-size simulations; black lines show simulation medians; and magenta lines show DMFT predictions. (c) Example showing correspondence between energy decay and overlap evolution for $n = 1, \alpha = 0.16$. Top: normalized overlap $\bar{m}(t)$; middle: energy $\varepsilon(t)$; bottom: energy derivative $d\varepsilon(t)/dt$. Horizontal axis shows time on log scale. The fast rise and slow decay of the normalized overlap correspond to fast decay and slow decay of the energy, consistent with the system navigating shallow energy landscape features near stored patterns that eventually drive it away from the memory. (d) Schematic of the slow energy landscape structure in the vicinity of stored patterns (bottom) that serves as a remnant of the stable basins that exist in the below-capacity regime (top).

All curves lie above the diagonal since $\bar{m}_{\text{max}} \geq \bar{m}_{\text{init}}$. When α is sufficiently small and \bar{m}_{init} is sufficiently large, the network enters a stable retrieval state. This is reflected by the curve becoming flat, i.e., \bar{m}_{max} becomes insensitive to local changes in \bar{m}_{init} . Below capacity but outside the basin of attraction, \bar{m}_{max} increases smoothly with \bar{m}_{init} until entering the basin, reflecting transient retrieval. Above the critical threshold, the entire curve shows smooth increases due to transient retrieval.

The transient-recovery curves reveal that going above capacity results in changes to retrieval performance that are far more graceful than equilibrium analyses suggest. As α increases from below to above critical capacity, the curves change smoothly rather than exhibiting abrupt discontinuities (of course, however, the presence or absence of a flat plateau represents a qualitative difference between the two regimes). Thus, the “blackout catastrophe” is considerably less catastrophic when viewed through transient dynamics. Networks retain substantial memory function even beyond their critical capacities, provided one accepts transient rather than persistent recall.

While comparing individual curves at fixed α across different n is not meaningful since α_c varies strongly with n , the families of curves generated by varying α can be compared. Comparing these families across interaction orders reveals important differences in transient retrieval characteristics. The Hopfield model exhibits the most graceful degradation, with curves that maintain roughly symmetric shape around the diagonal as α increases. In contrast, higher-order models show increasingly asymmetric behavior, with transient recovery effects becom-

ing most pronounced for large \bar{m}_{init} . This asymmetry is most extreme for $n = 4$, where large initial overlaps are required to obtain substantial transient retrieval. Conversely, the Hopfield model shows significant transient recovery even for modest initial overlaps.

E. Energy dynamics

The energy function provides another lens for understanding retrieval dynamics. We show that the transient retrieval phenomenon is caused by slow regions in the energy landscape near memories where, below capacity, stable fixed points previously existed.

Fig. 4a,b shows energy versus time for different initial overlaps, with columns representing $n = 1, 2, 4$ and (a) and (b) showing below- and above-capacity regimes, respectively. When entering stable retrieval states (below capacity with sufficient initial overlap), the energy quickly drops to a fixed value independent of the specific initial overlap. When displaying transient retrieval (above capacity or with small initial overlap), the energy exhibits two distinct timescales of decay: fast initial decay followed by slow decay. This slow decay corresponds to the system exploring regions of small gradient (i.e., slow regions) of the energy landscape.

The correspondence between energy and overlap dynamics is illustrated in Fig. 4c, which shows three complementary views: normalized overlap $\bar{m}(t)$ (top), energy $\varepsilon(t)$ (middle), and energy time derivative $d\varepsilon(t)/dt$ (bottom), all shown on a logarithmic time scale. The fast energy decay corresponds to the fast rise of $\bar{m}(t)$, while

the slow energy decay corresponds to the slow decay of $\bar{m}(t)$. This demonstrates that transient retrieval occurs when the system becomes trapped in slowly-varying regions of the energy landscape—remnants of the stable fixed points that existed below capacity. We schematize this landscape structure in Fig. 4d.

F. Optimal readout time

In networks storing memories as stable fixed points, memories can be read out at any sufficiently late time after convergence. However, when memories are retrieved via transient dynamics in slow regions of the energy landscape, there exists an optimal readout time that maximizes retrieval performance.

Fig. 5 plots the optimal readout time,

$$t_{\text{opt}} = \arg \max_t \bar{m}(t), \quad (67)$$

from the DMFT as a function of \bar{m}_{init} . Each row shows increasing values of α , with columns showing $n = 1, 2, 4$. When the network enters a stable retrieval state for sufficiently high \bar{m}_{init} below capacity, we shade the region and do not plot t_{opt} since no well-defined unique optimal time exists—any sufficiently late time yields the same high overlap.

In networks below capacity (with shaded regions), t_{opt} grows monotonically as \bar{m}_{init} approaches the basin boundary. This growth becomes rapid and possibly divergent (though we cannot confirm this due to T being finite in our solutions) as \bar{m}_{init} approaches the critical value for entering the basin of attraction.

In networks above capacity (without shaded regions), no basin of attraction exists and the optimal readout time curves become non-monotonic. t_{opt} increases for small \bar{m}_{init} , reaches a maximum at intermediate values—roughly where the below-capacity critical \bar{m}_{init} was located—then decreases back toward $t_{\text{opt}} = 0$ at $\bar{m}_{\text{init}} = 1$. This non-monotonic behavior reflects the remnant structure of the energy landscape: initial conditions with intermediate overlap can access the shallow remnants of the former basin, making it worthwhile to wait as the system exploits these landscape features to increase overlap before eventual decay. In contrast, initial conditions with very high overlap are already near optimal alignment, while those with very low overlap cannot effectively access the relevant landscape features. In these cases, there is little benefit to waiting, as the system either starts near its optimal retrieval performance or cannot meaningfully improve retrieval performance through transient dynamics.

V. DISCUSSION

While we have used the cavity method for its intuitive appeal and suitability to bipartite systems, most

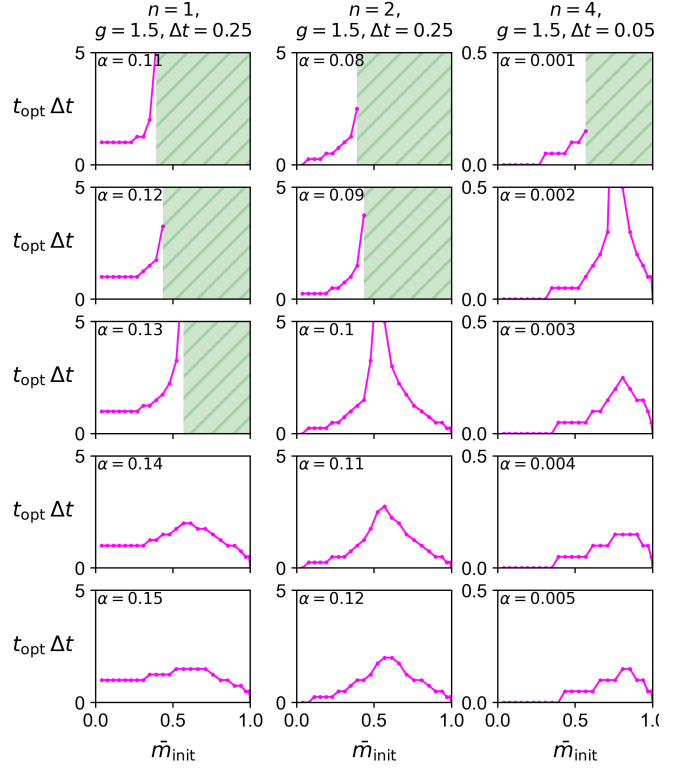


FIG. 5. Optimal readout time $t_{\text{opt}} = \arg \max_t \bar{m}(t)$ as a function of initial normalized overlap \bar{m}_{init} . Columns show $n = 1, 2, 4$ from left to right. Rows show increasing α values. **Magenta** lines show DMFT values of t_{opt} . **Green** shaded regions indicate where the network enters a stable retrieval state, making the optimal readout time undefined since any late time works equally well.

prior theoretical work on Hopfield dynamics has used path-integral approaches. One version of the path-integral approach, applicable to systems described by differential or difference equations (potentially with noise, e.g., Langevin dynamics), is known as the Martin–Siggia–Rose–De Dominicis–Janssen (MSRDJ) formalism [27–29]. This approach constructs a generating functional encoding correlation and response functions through its derivatives. The functional enforces the equations of motion using integral representations of delta functions. After averaging over the quenched disorder, order parameters are introduced that factor a resulting action across sites, allowing the order parameters to be determined by saddle point at large N . This formalism has been used extensively to study the dynamics of disordered systems. For instance, Sompolinsky and Zippelius [30] used it to study Langevin equations for a soft-spin version of the Sherrington–Kirkpatrick model, and it has found rich applications in disordered recurrent neural networks [31–33]. The path-integral formalism also enables analysis of fluctuations around the $N \rightarrow \infty$ values of the order parameters, allowing computation of quantities such as Lyapunov exponents [31] or the dimension of activity in random recurrent neural networks [21].

For discrete spins evolving at finite temperature, the natural description uses master equations (e.g., describing Glauber dynamics), and path-integral approaches have been developed for these systems as well. Sommers [34] developed one such method for the Sherrington-Kirkpatrick model, though this derivation was later questioned [35]. Nevertheless, this formalism became the foundation for subsequent work on Hopfield dynamics. Rieger *et al.* [36] used the Sommers formulation to study Hopfield dynamics but did not solve the dynamical equations, which would have required the kind of numerical scheme we use here, instead recovering replica-symmetric results of [3, 4] through long-time limits. A similar approach was taken by Horner *et al.* [37], who studied binary-spin Hopfield dynamics starting from a generating functional “derived from Langevin dynamics of soft spin variables or from Sommers’s formulation,” then solved the DMFT equations using approximation schemes. For a review of these methods, see Coolen and Sherrington [38] and more recently Coolen [39]. Another interesting work is that of Gardner *et al.* [40], who used essentially the MSRDJ formalism to study deterministic, discrete-time evolution of binary neurons in the Hopfield model (and Sherrington-Kirkpatrick model), deriving DMFT equations and analytically examining the first few time steps of retrieval.

Both Horner and Gardner noted, but did not explore in detail, the nonmonotonic nature of retrieval that is central to our work. Horner observed in the context of partial transient retrieval: “An initial increase of $m(t)$ is observed...This partial transient retrieval process is, however, not very efficient and is therefore not discussed further. Obviously the behavior at early times does not allow to draw conclusions whether a pattern is retrieved or not” (it is unclear what was meant by “not very efficient” given that the initial phase of transient retrieval is fast). Gardner made even more detailed observations about transient retrieval phenomena, noting that the overlap “is not always a monotonic function of time” and describing cases where “the configuration in the first time steps goes towards the pattern but at later times goes away.” She also observed transient retrieval due to initialization outside a basin of attraction, noting a case where “the system remembers after [1 or 2] time steps whereas at large time, the system remembers only if the initial overlap is sufficiently large.” An intriguing suggestion of Gardner’s was to exploit transient retrieval in below-capacity networks to ultimately land the system in a basin of attraction: “It might be possible after a few time steps of parallel iteration to define a way of annealing into a metastable state closer to the pattern.” This is an interesting future direction.

A rather different well-studied case of Hopfield network dynamics is that of randomly diluted networks, where a random mask is applied following Hebbian construction of the weights to zero out many connectivity entries [41–44]. In the limit where each neuron receives K inputs with $K \rightarrow \infty$, $N \rightarrow \infty$, and $K/N \rightarrow 0$, the preactivations

become Gaussian, allowing analytical solution similar to those for chaotic random recurrent networks [45].

A more esoteric but analytically tractable model of associative memory dynamics is that of [46], in which neuronal variables are constrained in their L2-norm rather than using a saturating nonlinearity, and interactions are four-way, since pairwise interactions in this model do not allow a retrieval phase. In this case, one can use generating functional (or, presumably, cavity) techniques to derive differential equations governing the evolution of the two-time order parameters. This approach is similar to that used for p -spin glass models, whose DMFT and aging behavior were studied by [47].

Our work builds on this history by deriving and providing a complete numerical solution of the DMFT equations for continuous-variable Hopfield and dense associative memory models. These models extend the theoretical framework to a more general class of associative memory models currently of interest in neuroscience and machine learning. The cavity method we use offers an intuitive, complementary perspective to the path-integral approaches that have dominated the field. Modern computational resources, particularly GPU acceleration, enable our numerical solution scheme, allowing investigation of the full temporal evolution of these complex systems rather than being limited to approximation schemes or the first couple of time steps.

Equipped with these DMFT solutions, we have taken a dynamical rather than an equilibrium perspective on associative memory models. While equilibrium analyses reveal the existence and stability of memory states, the dynamical view provides complementary insights into transient evolution, where much of the interesting memory retrieval actually occurs. We demonstrated that patterns can be transiently retrieved even when stable attractors no longer exist due to slow regions that persist in the energy landscape near stored patterns. The idea of using dynamics to probe energy landscape structure has precedent—Sompolinsky and colleagues [30, 48] famously used finite-temperature dynamics of soft-spin glass models to uncover the ultrametric energy-landscape structure underlying the replica solution.

The analytical and numerical DMFT tools developed here should be useful for analyzing other large recurrent neural networks where transient dynamics play important roles. For example, minor modifications of our equations and numerical techniques allow for determining order parameters in randomly connected recurrent neural networks with varying levels of reciprocal correlation, $\rho = \langle J_{ij} J_{ji} \rangle / \langle J_{ij}^2 \rangle$. This problem was studied in simulations by [49], and the mean-field theory was solved under the assumption of stationary dynamics (dependence of order parameters only on $t - t'$) by [50]. A similar approach was applied to the random Lotka-Volterra model in ecology by [18]. For $\rho = 1$, there exists a Lyapunov function and non-stationary behavior is guaranteed—such a system is analogous to zero-temperature dynamics in the Sherrington-Kirkpatrick model [30]. An open

question remains whether non-stationary behavior persists (rather than eventually equilibrating to a time-translation invariant state) only at $\rho = 1$, for all ρ above a critical $\rho_c > 0$, or for all $\rho > 0$.

Our analysis introduced transient-recovery curves (Sec. IV D) as a tool for characterizing retrieval performance without requiring stable states, revealing that transient recall behavior changes gracefully as capacity increases rather than exhibiting an abrupt breakdown. Methods for characterizing or reverse-engineering recurrent neural networks whose computations rely on transient dynamics remain nascent [16] compared to fixed point-based methods [14], and this area warrants further attention.

The optimal readout time t_{opt} before reading out a memory can be quite long, particularly when the system is initialized near the edge of a basin of attraction below capacity or when operating where this edge used to be just above capacity (Sec. IV F). In this regime, the network dynamics—not just the static information stored in the weights—play a crucial role in retrieval. Characterizing when recurrent dynamics are necessary for computation versus when feedforward processing suffices is an important question. An interesting recent study showed that in very sparsely connected networks designed to retrieve patterns, multiple timesteps of evolution are required for retrieval to allow information to propagate across the network, since most neurons are not directly connected [51].

Future work could extend our analysis to networks with structured rather than random patterns, which may exhibit different transient retrieval properties relevant for generalization. For instance, slow regions in the energy landscape might enable meaningful interpolation between data, potentially allowing networks to learn continuous manifold structure from discrete examples. This hypothesis is being explored in relation to diffusion models [52, 53] and has connections to associative memory [54].

We have considered noiseless dynamics. Understanding how noise affects transient retrieval could reveal new regimes of memory function and provide insights into the robustness of biological memory systems. An interesting example is the work of [55], who showed that temporal correlations in noise can improve retrieval in the higher-order spherical generalization of the Hopfield model by [46].

Finally, neuroscience experiments could potentially test whether biological neural networks exploit transient dynamics for memory retrieval, as our results suggest they could. Experimental signatures of this phenomenon could be detected through analysis of neural population activity during memory tasks. Specifically, one could compute time-varying similarity measures between population activity and stored memory patterns, analogous to our overlap function $m(t)$. The presence of transient retrieval would manifest as initial increases in pattern similarity followed by slower decay. Observing this on

error trials would be a particularly compelling connection to behavior.

VI. ACKNOWLEDGMENTS

The author thanks L.F. Abbott, Ken Miller, Stefano Fusi, Ashok Litwin-Kumar, and Haim Sompolinsky for useful discussions, comments, and pointers. The author was supported by the Gatsby Charitable Foundation and the Kavli Foundation.

Appendix A: Numerically stable $F(\phi)$

For $\phi(x) = \tanh(x)$, $F(\phi)$ can be evaluated in a numerically stable manner using

$$F(\phi) = \frac{1}{2} \log(1 - \phi^2) + x\phi \quad (\text{A1})$$

$$= \log 2 + x - \text{SoftPlus}(2x) + x\phi, \quad (\text{A2})$$

where $\tanh x = \phi$ and $\text{SoftPlus}(x) = \log(1 + e^x)$ has numerically stable implementations in common libraries.

Appendix B: Fixed-point mean-field theory and critical capacities

For completeness, we derive the fixed-point mean-field theory that yields the critical capacities reported in the main text. Equilibrium properties of the Hopfield model were computed using the replica method by Kühn *et al.* [19], and our results for $n = 1$ should agree with this analysis. Here we obtain the fixed-point statistics for general n by taking the static limit of our DMFT cavity equations. This analysis confirms that the model reproduces the “blackout catastrophe”—the discontinuous vanishing of the nonzero overlap solution.

For a single condensed pattern, the equilibrium single-site equations are obtained by removing time dependence from the DMFT equations. This gives the self-consistent system

$$x = \frac{g}{\sqrt{\alpha}} \xi m^n + \eta + F\phi(x), \quad (\text{B1})$$

$$m = \langle \xi \phi(x) \rangle_{\substack{\text{single-} \\ \text{site}}}, \quad (\text{B2})$$

$$C^\phi = \langle \phi^2(x) \rangle_{\substack{\text{single-} \\ \text{site}}}, \quad (\text{B3})$$

$$S^\phi = \left\langle \frac{\phi'(x)}{1 - F\phi'(x)} \right\rangle_{\substack{\text{single-} \\ \text{site}}}, \quad (\text{B4})$$

where we have dropped the subscript 0 for brevity and set $\sigma_\xi = 1$. The cavity field variance and self-coupling

kernel are given by

$$C^\eta = \begin{cases} g^2 K^2 C^\phi & n = 1 \\ (2n-1)!! g^2 (C^\phi)^n & n > 1, \text{ even} \end{cases} \quad (\text{B5})$$

$$F = \begin{cases} g\sqrt{\alpha}K & n = 1 \\ n(2n-1) \cdot (2n-3)!! g^2 S^\phi (C^\phi)^{n-1} & n > 1, \text{ even} \end{cases} \quad (\text{B6})$$

where for the Hopfield case ($n = 1$), we have defined

$$K = \frac{1}{1 - \frac{g}{\sqrt{\alpha}} S^\phi}. \quad (\text{B7})$$

The single-site average $\langle \cdot \rangle_{\text{single-site}}$ involves sampling $\xi \sim P(\xi)$ and $\eta \sim \mathcal{N}(0, C^\eta)$, then solving for x according to the nonlinear equation [Eq. B1](#).

Using $\phi(x) = \tanh(x)$, a technical issue arises when $F \geq 1$, as the equation $x = F\phi(x) + A$ (where $A = \frac{g}{\sqrt{\alpha}}\xi m^n + \eta$) can have multiple solutions for a range of A values. This issue is resolved in the replica approach by requiring that the chosen solution minimizes a certain energy function [\[19\]](#). There should be a way to recover this prescription in the cavity approach, making our equations agree with those of Kühn *et al.* [\[19\]](#) for $n = 1$ in our theory and temperature $\rightarrow 0$ in theirs, modulo self-interactions, but it is not immediately obvious how to do this.

To sidestep this multiple-solution issue, we restrict our analysis to $g = 1.5$, for which we find that F remains substantially below unity until the overlap solution m abruptly vanishes with increasing α . This allows us to compute the critical capacities where the high-overlap solution disappears ([Table I](#)).

Interaction order n	Critical capacity α_c (at $g = 1.5$)
1	0.13
2	0.080
4	0.0011

TABLE I. Critical capacities at $g = 1.5$.

Appendix C: Effects of g and Δt

The transient retrieval phenomenology depends on the model parameters g and Δt . [Fig. 6](#) explores how varying these parameters affects transient retrieval through transient-recovery curves for the Hopfield model. Once g reaches ~ 3 , the curves largely converge. No clear trends are visible regarding Δt .

Appendix D: Odd n and scaling behavior

To demonstrate the divergent behavior that occurs with odd n , we compute synthetic neuronal inputs,

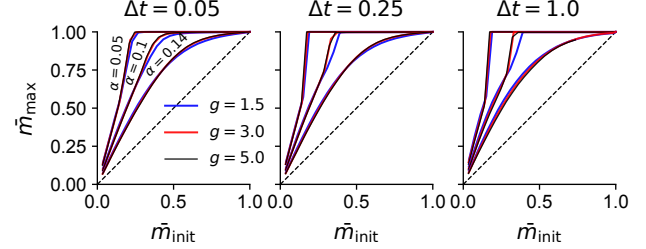


FIG. 6. Effects of gain g and time step Δt on transient retrieval dynamics for the Hopfield model ($n = 1$). Three panels from left to right show $\Delta t = 0.05, 0.25, 1.0$. Transient-recovery curves are shown for $\alpha = 0.05, 0.1, 0.14$, with gain values $g = 1.5, 3, 5$ distinguished by different colors for each α . Axes show maximum normalized overlap \bar{m}_{max} versus initial normalized overlap \bar{m}_{init} as in [Fig. 3](#). Curves for different gain values at the same α are closely grouped.

$\text{input}_i = \frac{1}{\sqrt{\alpha}} \sum_\mu \xi_i^\mu (m^\mu)^n$, where $m^\mu = \frac{1}{N} \sum_i \xi_i^\mu \phi_i$ and both ξ_i^μ and ϕ_i are i.i.d. ± 1 . We use $\alpha = 0.01$ and $P = \alpha N^n$. We compute this for each combination of $N \in \{25, 75, 125, 175\}$ and $n \in \{1, 2, 3, 4\}$. The mean and standard deviation of the neuronal input across the i index for a single draw of all variables are plotted in [Fig. 7](#). With increasing N , the standard deviations remain flat (consistent with proper scaling) for all cases except $n = 3$, which grows linearly with N .

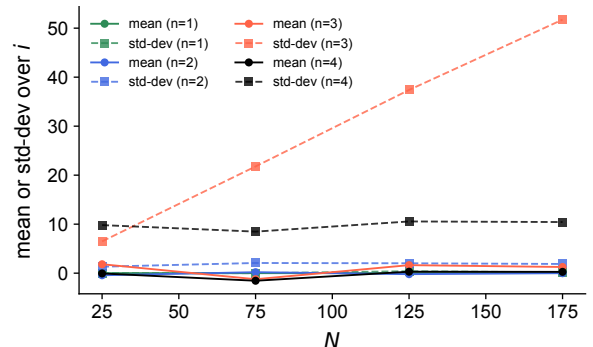


FIG. 7. Demonstration of divergent behavior for odd interaction orders. Mean and standard deviation of neuronal input $\text{input}_i = \frac{1}{\sqrt{\alpha}} \sum_\mu \xi_i^\mu (m^\mu)^n$ as functions of system size N for interaction orders $n = 1, 2, 3, 4$.

[1] J. J. Hopfield, Neural networks and physical systems with emergent collective computational abilities., *Proceedings*

of the national academy of sciences **79**, 2554 (1982).

[2] J. J. Hopfield, Neurons with graded response have collective computational properties like those of two-state neurons., *Proceedings of the national academy of sciences* **81**, 3088 (1984).

[3] D. J. Amit, H. Gutfreund, and H. Sompolinsky, Storing infinite numbers of patterns in a spin-glass model of neural networks, *Physical Review Letters* **55**, 1530 (1985).

[4] D. J. Amit, H. Gutfreund, and H. Sompolinsky, Statistical mechanics of neural networks near saturation, *Annals of physics* **173**, 30 (1987).

[5] D. Tyulmankov, Computational models of learning and synaptic plasticity, *arXiv preprint arXiv:2412.05501* (2024).

[6] F. Zenke and A. Laborieux, Theories of synaptic memory consolidation and intelligent plasticity for continual learning, *arXiv preprint arXiv:2405.16922* (2024).

[7] D. Krotov and J. J. Hopfield, Dense associative memory for pattern recognition, *Advances in neural information processing systems* **29** (2016).

[8] D. Krotov and J. Hopfield, Large associative memory problem in neurobiology and machine learning, *arXiv preprint arXiv:2008.06996* (2020).

[9] L. F. Abbott and Y. Arian, Storage capacity of generalized networks, *Physical review A* **36**, 5091 (1987).

[10] E. Gardner, Multiconnected neural network models, *Journal of Physics A: Mathematical and General* **20**, 3453 (1987).

[11] D. Horn and M. Usher, Capacities of multiconnected memory models, *Journal de Physique* **49**, 389 (1988).

[12] H. Chen, Y. Lee, G. Sun, H. Lee, T. Maxwell, and C. L. Giles, High order correlation model for associative memory, in *AIP Conference Proceedings*, Vol. 151 (American Institute of Physics, 1986) pp. 86–99.

[13] L. Kozachkov, J.-J. Slotine, and D. Krotov, Neuron-astrocyte associative memory, *Proceedings of the National Academy of Sciences* **122**, e2417788122 (2025).

[14] N. Maheswaranathan, A. Williams, M. Golub, S. Ganguli, and D. Sussillo, Universality and individuality in neural dynamics across large populations of recurrent networks, *Advances in neural information processing systems* **32** (2019).

[15] S. Vyas, M. D. Golub, D. Sussillo, and K. V. Shenoy, Computation through neural population dynamics, *Annual review of neuroscience* **43**, 249 (2020).

[16] E. Turner, K. V. Dabholkar, and O. Barak, Charting and navigating the space of solutions for recurrent neural networks, *Advances in Neural Information Processing Systems* **34**, 25320 (2021).

[17] While preparing this manuscript, Mimura *et al.* [56] derived related equations for binary-spin dense associative memory networks using generating functional methods. In contrast to our work, they studied binary rather than graded-activity networks, used generating functionals rather than bipartite cavity methods, did not attempt to solve the equations numerically, did not analyze transient retrieval or energy dynamics, and did not compare their results to finite-size simulations.

[18] F. Roy, G. Biroli, G. Bunin, and C. Cammarota, Numerical implementation of dynamical mean field theory for disordered systems: Application to the lotka–volterra model of ecosystems, *Journal of Physics A: Mathematical and Theoretical* **52**, 484001 (2019).

[19] R. Kühn, S. Bös, and J. L. van Hemmen, Statistical mechanics for networks of graded-response neurons, *Physical Review A* **43**, 2084 (1991).

[20] A. van Meegen and H. Sompolinsky, Coding schemes in neural networks learning classification tasks, *Nature Communications* **16**, 3354 (2025).

[21] D. G. Clark, O. Marschall, A. van Meegen, and A. Litwin-Kumar, Connectivity structure and dynamics of nonlinear recurrent neural networks, *arXiv preprint arXiv:2409.01969* (2024).

[22] D. G. Clark and H. Sompolinsky, Simplified derivations for high-dimensional convex learning problems, *arXiv preprint arXiv:2412.01110* (2024).

[23] M. Mézard and G. Parisi, The cavity method at zero temperature, *Journal of Statistical Physics* **111**, 1 (2003).

[24] M. Ramezanali, P. P. Mitra, and A. M. Sengupta, The cavity method for analysis of large-scale penalized regression, *arXiv preprint arXiv:1501.03194* (2015).

[25] J. W. Rocks and P. Mehta, Memorizing without overfitting: Bias, variance, and interpolation in overparameterized models, *Physical review research* **4**, 013201 (2022).

[26] M. Shamir and H. Sompolinsky, Thouless-anderson-palmer equations for neural networks, *Physical Review E* **61**, 1839 (2000).

[27] P. C. Martin, E. D. Siggia, and H. A. Rose, Statistical dynamics of classical systems, *Physical Review A* **8**, 423 (1973).

[28] C. De Dominicis, Dynamics as a substitute for replicas in systems with quenched random impurities, *Physical Review B* **18**, 4913 (1978).

[29] J. A. Hertz, Y. Roudi, and P. Sollich, Path integral methods for the dynamics of stochastic and disordered systems, *Journal of Physics A: Mathematical and Theoretical* **50**, 033001 (2016).

[30] H. Sompolinsky and A. Zippelius, Relaxational dynamics of the edwards-anderson model and the mean-field theory of spin-glasses, *Physical Review B* **25**, 6860 (1982).

[31] A. Crisanti and H. Sompolinsky, Path integral approach to random neural networks, *Physical Review E* **98**, 062120 (2018).

[32] M. Helias and D. Dahmen, *Statistical field theory for neural networks*, Vol. 970 (Springer, 2020).

[33] W. Zou and H. Huang, Introduction to dynamical mean-field theory of randomly connected neural networks with bidirectionally correlated couplings, *SciPost Physics Lecture Notes* , 079 (2024).

[34] H.-J. Sommers, Path-integral approach to ising spin-glass dynamics, *Physical review letters* **58**, 1268 (1987).

[35] A. Lusakowski, Comment on “path-integral approach to ising spin-glass dynamics.”, *Physical Review Letters* **66**, 2543 (1991).

[36] H. Rieger, M. Schreckenberg, and J. Zittartz, Glauber dynamics of the little-hopfield model, *Zeitschrift für Physik B Condensed Matter* **72**, 523 (1988).

[37] H. Horner, D. Bormann, M. Frick, H. Kinzelbach, and A. Schmidt, Transients and basins of attraction in neural network models, *Zeitschrift für Physik B Condensed Matter* **76**, 381 (1989).

[38] T. Coolen and D. Sherrington, Dynamics of attractor neural networks, *Mathematical Approaches to Neural Networks*, Elsevier **51**, 293 (1993).

[39] A. Coolen, Statistical mechanics of recurrent neural networks ii—dynamics, in *Handbook of biological physics*, Vol. 4 (Elsevier, 2001) pp. 619–684.

[40] E. Gardner, B. Derrida, and P. Mottishaw, Zero temperature parallel dynamics for infinite range spin glasses and

neural networks, *Journal de physique* **48**, 741 (1987).

[41] B. Derrida, E. Gardner, and A. Zippelius, An exactly solvable asymmetric neural network model, *Europhysics Letters* **4**, 167 (1987).

[42] B. Derrida and J. Nadal, Learning and forgetting on asymmetric, diluted neural networks, *Journal of statistical physics* **49**, 993 (1987).

[43] B. Tirozzi and M. Tsodyks, Chaos in highly diluted neural networks, *Europhysics Letters* **14**, 727 (1991).

[44] U. Pereira-Obilinovic, J. Aljadeff, and N. Brunel, Forgetting leads to chaos in attractor networks, *Physical Review X* **13**, 011009 (2023).

[45] H. Sompolinsky, A. Crisanti, and H.-J. Sommers, Chaos in random neural networks, *Physical review letters* **61**, 259 (1988).

[46] D. Bollé, T. M. Nieuwenhuizen, I. P. Castillo, and T. Verbeiren, A spherical hopfield model, *Journal of Physics A: Mathematical and General* **36**, 10269 (2003).

[47] A. Altieri, G. Biroli, and C. Cammarota, Dynamical mean-field theory and aging dynamics, *Journal of Physics A: Mathematical and Theoretical* **53**, 375006 (2020).

[48] H. Sompolinsky, Time-dependent order parameters in spin-glasses, *Physical Review Letters* **47**, 935 (1981).

[49] D. Martí, N. Brunel, and S. Ostoic, Correlations between synapses in pairs of neurons slow down dynamics in randomly connected neural networks, *Physical Review E* **97**, 062314 (2018).

[50] D. G. Clark, L. Abbott, and A. Litwin-Kumar, Dimension of activity in random neural networks, *Physical Review Letters* **131**, 118401 (2023).

[51] D. Turcu and L. Abbott, Sparse rnns can support high-capacity classification, *PLOS Computational Biology* **18**, e1010759 (2022).

[52] Z. Kadkhodaie, F. Guth, E. P. Simoncelli, and S. Mallat, Generalization in diffusion models arises from geometry-adaptive harmonic representations, *arXiv preprint arXiv:2310.02557* (2023).

[53] M. Kamb and S. Ganguli, An analytic theory of creativity in convolutional diffusion models, *arXiv preprint arXiv:2412.20292* (2024).

[54] B. Pham, G. Raya, M. Negri, M. J. Zaki, L. Ambrogioni, and D. Krotov, Memorization to generalization: Emergence of diffusion models from associative memory, *arXiv preprint arXiv:2505.21777* (2025).

[55] A. K. Behera, M. Rao, S. Sastry, and S. Vaikuntanathan, Enhanced associative memory, classification, and learning with active dynamics, *Physical Review X* **13**, 041043 (2023).

[56] K. Mimura, J. Takeuchi, Y. Sumikawa, Y. Kabashima, and A. C. C. Coolen, Dynamical properties of dense associative memory, *arXiv preprint arXiv:2506.00851* (2025).